Vilnius
University
Press

Effect of gravity on the pattern formation in aqueous suspensions of luminous *Escherichia coli*

Boleslovas Dapkūnas[a] , **Romas Baronas**[a] , **Remigijus Šimkus**[b]

[a] Vilnius University, Faculty of Mathematics and Informatics,
Institute of Computer Science,
Didlaukio g. 47, LT-08303 Vilnius, Lithuania
boleslovas.dapkunas@mif.vu.lt

[b] Vilnius University, Life Sciences Center, Institute of Biochemistry,
Saulėtekio al. 7, LT-10257 Vilnius, Lithuania

Abstract. This paper presents a nonlinear two-dimensional-in-space mathematical model of self-organization of aqueous bacterial suspensions. The reaction–diffusion–chemotaxis model is coupled with the incompressible Navier–Stokes equations, which are subject to a gravitational force proportional to the relative bacteria density and include a cut-off mechanism. The bacterial pattern formation of luminous *Escherichia coli* is modelled near the inner lateral surface of a circular micro-container, as detected by bioluminescence imaging. The simulated plume-like patterns are analysed to determine the values of the dimensionless model parameters, the Schmidt number, Rayleigh number and oxygen cut-off threshold, that closely match the patterns observed experimentally in a luminous *E. coli* colony. The numerical simulation at the transient conditions was carried out using the finite difference technique.

Keywords: chemotaxis, reaction–diffusion, bioconvection, pattern formation, mathematical modelling.

1 Introduction

Bacteria are capable of detecting gradients of chemical signals in their environment and direct their movement according to such gradients, forming millimeter-scale patterns and exhibiting strong inhomogeneity in their density, mainly near contact lines and surfaces [9, 11, 12, 56]. The interaction of different processes in suspensions of bacteria such as *Escherichia coli* results in complex dynamic systems [49, 57, 59].

The directed movement of microorganisms including bacteria in response to chemical gradients is called chemotaxis [18]. *E. coli* is capable not only to move up gradients of attractants and down gradients of repellents, but also to seek optimal conditions of pH, osmolarity and oxygen concentration as well as to avoid noxious substances and crowding [1, 2, 47].

Mathematical and computational modelling are contributing significantly to understanding how bacteria read, respond to and shape the sensory information in their environment [21,26,40]. Although a number of models based on reaction–advection–diffusion equations have been developed, the system introduced by Keller and Segel remains among the most widely used [4, 8, 13, 17, 21, 40]. The classical Keller–Segel model describes the dynamics of bacteria, chemoattractant and nutrient by a system of nonlinear equations of the reaction–diffusion–chemotaxis type [29, 30].

The Keller–Segel approach was also applied to investigate the bacterial self-organization as experimentally detected by bioluminescence imaging [6,7,48,49,52]. The nonlinear two-dimensional-in-space model was used to simulate the pattern formation in the liquid cultures of bacteria near the inner lateral surface of a circular micro-container [6,49]. Different functions modulating the rates of cell growth, the chemoattractant production and the oxygen (nutrient) consumption were applied in modelling the bacterial population dynamics [10, 19, 54, 56]. Although the simulated two-dimensional bamboo foam-like structures were similar to the experimentally observed structures, the vertical as well as horizontal distributions of cells were noticeably different from those noticed in physical experiments where azimuthal waves or falling plumes were additionally observed [49–51].

Hillesdon et al. coupled the Keller–Segel model with the fluid flow equation to model the pattern formation in suspensions of swimming bacteria of the species *Bacillus subtilis* in an incompressible fluid [24]. Aquatic bacteria like *Bacillus subtilis* swim upwards through a response to oxygen (aerotaxis), which they consume. The mass of bacteria generates a gravitational force that leads to Rayleigh–Taylor instability, causing bioconvection and forming structures such as falling plumes [3, 13, 15, 24, 56]. Tuval et al. demonstrated the self-organized formation of a persistent hydrodynamic vortex that traps cells near the contact line in suspensions of *Bacillus subtilis* [56]. *E. coli* also consumes oxygen but swims to self-excreted chemoattractant (chemotaxis) [12, 58]. Plumes and bioconvection patterns have also been experimentally observed in suspensions of different swimming microorganisms, as well as even nonmotile bacteria, and modelled coupling the Navier–Stokes equation with advection–diffusion equations [16, 25, 41, 45]. The hydrodynamic phenomena in suspensions of swimming bacteria and other microorganisms were mathematically substantiated by Pedley and Kessler [41].

An analysis of the chemotaxis–diffusion–convection system showed that the instability condition significantly depends on the bioconvection (taxis) Rayleigh number [15,23]. The bioconvection Rayleigh number is defined as the ratio of buoyancy and viscosity forces, multiplied by the ratio of momentum and cell diffusivity, although the exact expression may vary [15, 23, 39, 41]. The viscosity forces, which play a key role in the dimensionless Rayleigh number, are related to the fluid's kinematic viscosity, which determines the strength and range of bacterial interactions with the surrounding fluid through hydrodynamic forces [25, 34]. The kinematic viscosity is also involved in the dimensionless Schmidt number, which relates the diffusivity of momentum (kinematic viscosity) to the diffusivity of mass such as bacteria [25, 34].

Recent studies have shown the importance of a cut-off mechanism for modelling in the bacterial pattern formation, as the bacterial activity ceases when the oxygen concentration

falls below a critical cut-off value [13, 19, 45, 56]. The cut-off mechanism was particularly used to limit the chemoattractant emission [55, 61] and is typically modelled by the Heaviside step function [35, 43, 54, 55].

The aim of this work was to improve the reaction–diffusion–chemotaxis model, which involves the dynamics of bacterial density, the concentration of self-excreted chemoattractant and oxygen concentration [6, 49, 52], by coupling the model with the cut-off mechanism and the incompressible Navier–Stokes equations, subject to a gravitational force proportional to the relative bacterial density [13, 24, 56]. Additionally, the work sought to investigate the influence of gravity and cut-off mechanism on the spatiotemporal pattern formation. In order to investigate the effects of gravity and the cut-off mechanism, bacterial patterns were simulated for different values of three parameters of the dimensionless governing equations: the Schmidt number, Rayleigh number and oxygen cut-off threshold. The nonlinear two-dimensional-in-space model was used to simulate the pattern formation in the liquid cultures of bacteria near the inner lateral surface of a circular micro-container. The simulated patterns were analysed in order to determine the values of the model parameters closely matching patterns experimentally observed in a luminous *E. coli* colony [49–52]. The numerical simulation at the transient conditions was carried out using the finite difference technique [6, 13, 46].

2 Mathematical modelling

2.1 Governing equations

The dynamics of bacteria, chemoattractant and oxygen have been modelled mathematically by the reaction–diffusion–chemotaxis equations [12, 57–59]. The pattern formation in an aqueous suspension of luminous *E. coli* near the inner lateral surface of a circular micro-container was described in the two-dimensional Cartesian system [6, 49, 52]. Assuming that the bacterial circulation is affected by the downward gravitational forcing leads to coupling the model with the incompressible Navier–Stokes equations subject to a gravitational force proportional to the relative bacteria density [13, 24, 32, 56]. The resulting coupled system of reaction–diffusion–chemotaxis–convection equations can be written as follows:

$$\frac{\partial n}{\partial t} + \boldsymbol{u} \cdot \boldsymbol{\nabla} n = D_n \Delta n - \nabla(k_1 n \nabla c) + k_2 n \left(1 - \frac{n}{k_3 o}\right), \tag{1_1}$$

$$\frac{\partial c}{\partial t} + \boldsymbol{u} \cdot \boldsymbol{\nabla} c = D_c \Delta c + \frac{k_4 n}{k_5 + n} r(o) - k_6 c, \tag{1_2}$$

$$\frac{\partial o}{\partial t} + \boldsymbol{u} \cdot \boldsymbol{\nabla} o = D_o \Delta o - k_7 n, \tag{1_3}$$

$$\rho\left(\frac{\partial \boldsymbol{u}}{\partial t} + \boldsymbol{u} \cdot \boldsymbol{\nabla} \boldsymbol{u}\right) = \nu \nabla^2 \boldsymbol{u} - \nabla p - n V_b g (\rho_b - \rho) \boldsymbol{j}, \tag{1_4}$$

$$\boldsymbol{\nabla} \cdot \boldsymbol{u} = 0, \qquad (x, y) \in (0, l) \times (0, h) \quad t > 0, \tag{1_5}$$

where Δ is the Laplacian in the Cartesian coordinates x and y, t stands for time, $n(x, y, t)$ denotes the cell density, $c(x, y, t)$ is the chemoattractant concentration, $o(x, y, t)$ is the oxygen concentration, $\boldsymbol{u} = (u_x(x, y, t), u_y(x, y, t))$ denotes the velocity field of water, u_x and u_y are the horizontal and vertical components of the vector $\boldsymbol{u}$, p is the pressure, ρ and ν are the fluid density and (dynamic) viscosity, ρ_b and V_b are the mass density and volume of bacteria, $g \approx 9.8$ m/s^2 is the gravitational acceleration, $\boldsymbol{j}$ is the upwards unit vector, D_n, D_c and D_o are the constant diffusion coefficients, $r(o)$ is the cut-off function for chemoattractant production, k_1 is the chemotactic sensitivity, k_2 denotes the population growth rate, k_3 stands for the linear dependence of bacterial carrying capacity on the oxygen concentration, k_4 and k_5 stand for the saturating chemoattractant production, k_6 denotes the chemoattractant degradation, k_7 is the rate of oxygen consumption by bacteria, l is the circumference of the cylinder base, and h is the height of the cylinder [6, 24, 49, 54, 56–59]. Subject to incompressibility, defined by (1_5), the fluid equation (1_4) uses the Boussinesq approximation in which the density variations caused by bacteria appear only in the buoyant forcing.

The term $V_b g(\rho_b - \rho)\boldsymbol{j}$ in (1_4) describes the gravitational force exerted by a bacterium on the fluid along the upward unit vector $\boldsymbol{j}$. Since bacteria are only about 10% denser than water and are diluted in the solvent, $nV_b(\rho_b - \rho)/\rho \ll 1$ [13, 15, 16, 24, 32, 56].

Physical experiments showed that the peak of bacterial concentration is just below the upper surface of the solution [19, 50]. To simulate this, a cut-off function $r(o)$ for chemoattractant production was introduced into the mathematical model. In this case, $r(o)$ models a threshold of partial inactivity of the bacteria due to the extremely high oxygen supply. The cut-off function $r(o)$ is typically modelled by the Heaviside step function $\Theta(o_{\max} - o)$ [43, 55], where $o_{\max}$ is the maximal oxygen concentration at which chemoattractant is excreted ($o_{\max} \leqslant o_0$). When oxygen concentration is above the cut-off point $o_{\max}$, chemoattractant is not produced, and bacteria move towards higher chemoattractant concentration. Since the oxygen concentration at the top of the surface is equal to o_0, this forces bacteria to move just below the surface. A cut-off function has already been applied to model the bacterial self-emission of the chemoattractant [55, 61]. This mechanism was also similarly used to model an insensitivity threshold in bacteria [13, 27, 56].

2.2   Initial and boundary conditions

The governing equations (1) are considered subject to the initial and boundary conditions to form an initial-boundary value problem. Possibly non-uniform distributions of cells, chemoattractant, oxygen and fluid velocity are assumed in the initial conditions ($t = 0$) [6, 49, 52, 56],

$$n(x, y, 0) = n_0(x, y), \quad c(x, y, 0) = c_0(x, y), \quad o(x, y, 0) = o_0(x, y),$$
$$\boldsymbol{u}(x, y, 0) = \boldsymbol{u}_0(x, y), \quad (x, y) \in [0, l] \times [0, h]. \tag{2}$$

Although the pattern formation, including falling bacterial plumes, is sometimes mathematically analysed assuming different regular initial conditions [13, 31, 32, 45], a small random initial perturbation of cells is required to obtain patterns similar to those

experimentally observed due to the non-zero initial velocity field usually present in the experimental set up [13, 15, 45].

At the top surface, the liquid medium comes into contact with the atmosphere, which contains oxygen, and the oxygen dissolves into the liquid until it reaches saturation. There is no flux of cells as well as of the chemoattractant, and the vertical fluid velocity and the tangential fluid stress are assumed zero ($t > 0$),

$$\left.\frac{\partial n}{\partial y}\right|_{y=h} = \left.\frac{\partial c}{\partial y}\right|_{y=h} = \left.\frac{\partial u_x}{\partial y}\right|_{y=h} = 0,$$

$$u_y(x, h, t) = 0, \quad o(x, h, t) = \bar{o}_0, \quad x \in [0, l], \tag{3}$$

where $\bar{o}_0$ is the saturation concentration of oxygen in the liquid medium.

The zero-flux boundary condition is applied for all the species, and the fluid velocity is supposed zero on the base of the glass vessel ($t > 0$),

$$\left.\frac{\partial n}{\partial y}\right|_{y=0} = \left.\frac{\partial c}{\partial y}\right|_{y=0} = \left.\frac{\partial o}{\partial y}\right|_{y=0} = 0, \quad \boldsymbol{u}(x, 0, t) = 0, \quad x \in [0, l]. \tag{4}$$

Due to the continuity of the lateral surface in the x-direction, the periodicity condition is applied on sides of the domain ($t > 0$, $y \in [0, h]$),

$$\left.\frac{\partial n}{\partial x}\right|_{x=0} = \left.\frac{\partial n}{\partial x}\right|_{x=l}, \quad n(0, y, t) = n(l, y, t), \tag{5$_1$}$$

$$\left.\frac{\partial c}{\partial x}\right|_{x=0} = \left.\frac{\partial c}{\partial x}\right|_{x=l}, \quad c(0, y, t) = c(l, y, t), \tag{5$_2$}$$

$$\left.\frac{\partial o}{\partial x}\right|_{x=0} = \left.\frac{\partial o}{\partial x}\right|_{x=l}, \quad o(0, y, t) = o(l, y, t), \tag{5$_3$}$$

$$\left.\frac{\partial u_x}{\partial x}\right|_{x=0} = \left.\frac{\partial u_x}{\partial x}\right|_{x=l}, \quad u_x(0, y, t) = u_x(l, y, t), \tag{5$_4$}$$

$$\left.\frac{\partial u_y}{\partial x}\right|_{x=0} = \left.\frac{\partial u_y}{\partial x}\right|_{x=l}, \quad u_y(0, y, t) = u_y(l, y, t). \tag{5$_5$}$$

2.3 Dimensionless model

A dimensionless mathematical model must be derived to obtain the main governing parameters of the mathematical model (1)–(5) [21,36,38]. The dimensionless variables were derived similarly to those in [6, 13, 24, 32, 56],

$$n^* = \frac{n}{n_0}, \quad c^* = \frac{k_5 k_6 c}{k_4 n_0}, \quad o^* = \frac{k_3 o}{n_0}, \quad \boldsymbol{u}^* = \frac{\boldsymbol{u}}{\sqrt{k_6 D_c}}, \quad t^* = k_6 t,$$

$$x^* = \sqrt{\frac{k_6}{D_c}} x, \quad y^* = \sqrt{\frac{k_6}{D_c}} y, \quad l^* = \sqrt{\frac{k_6}{D_c}} l, \quad h^* = \sqrt{\frac{k_6}{D_c}} h,$$

$$D_n^* = \frac{D_n}{D_c}, \quad D_o^* = \frac{D_o}{D_c}, \quad \chi = \frac{k_1 k_4 n_0}{k_5 k_6 D_c}, \quad \alpha = \frac{k_2}{k_6}, \quad \beta = \frac{n_0}{k_5},$$

$$\lambda = \frac{k_7 k_3}{k_6}, \quad \nu^* = \frac{\nu}{\rho D_c}, \quad \kappa = \frac{n_0 V_b g (\rho_b - \rho) \sqrt{D_c}}{\nu k_6 \sqrt{k_6}}.$$

This scale was chosen for consistency and comparison with previously published work [6,49]. After dropping the asterisks from the dimensionless variables, the fluid equation is rewritten in the stream function-vorticity formulation by introducing the vorticity and stream function. The governing equations (1) then take the following dimensionless form:

$$\frac{\partial n}{\partial t} + \boldsymbol{u} \cdot \boldsymbol{\nabla} n = D_n \Delta n - \chi \nabla(n \nabla c) + \alpha n \left(1 - \frac{n}{o}\right), \tag{6_1}$$

$$\frac{\partial c}{\partial t} + \boldsymbol{u} \cdot \boldsymbol{\nabla} c = \Delta c + \frac{n}{1 + \beta n} \Theta(o_{\max} - o) - c, \tag{6_2}$$

$$\frac{\partial o}{\partial t} + \boldsymbol{u} \cdot \boldsymbol{\nabla} o = D_o \Delta o - \lambda n, \tag{6_3}$$

$$\frac{\partial \omega}{\partial t} + \boldsymbol{u} \cdot \boldsymbol{\nabla} \omega = \nu \Delta \omega - \kappa \nu \frac{\partial n}{\partial x}, \tag{6_4}$$

$$\Delta \Psi = -\omega, \qquad (x, y) \in (0, l) \times (0, h) \quad t > 0, \tag{6_5}$$

where ω is the vorticity vector, and Ψ is the stream function defined as follows [13]:

$$\omega = \frac{\partial u_y}{\partial x} - \frac{\partial u_x}{\partial y}, \quad u_x = \frac{\partial \Psi}{\partial y}, \quad u_y = -\frac{\partial \Psi}{\partial x}. \tag{7}$$

The form of the initial (2) and boundary (3)–(5) conditions remains unchanged; however, all the model parameters and variables are now treated as dimensionless.

After transforming the model to the dimensionless form, ν denotes the Schmidt number, κ can be considered as the Rayleigh number, and the product $\kappa \nu$ represents the gravitational forces affecting the fluid [15, 34, 39, 41, 53].

3 Numerical simulation

Due to the nonlinearity of the governing equations (6), the initial boundary value problem (6)–(7), (2)–(5) was solved numerically using the finite difference technique [46]. The problem was discretized using a uniform grid of 250×112 points in the x and y dimensions, respectively, and a constant dimensionless time step in the interval $[2 \cdot 10^{-4}, 5 \cdot 10^{-4}]$ depending on the value of parameter ν was used. The alternating-direction implicit method was used to solve the problem [44, 46]. The diffusion terms were treated implicitly, while the other terms were treated explicitly. The Poisson equation (6_5) was solved using successive over-relaxation method [44]. The simulations were performed using software written by the authors in the Python programming language using the NumPy package, and the results were visualised using the Matplotlib package [28].
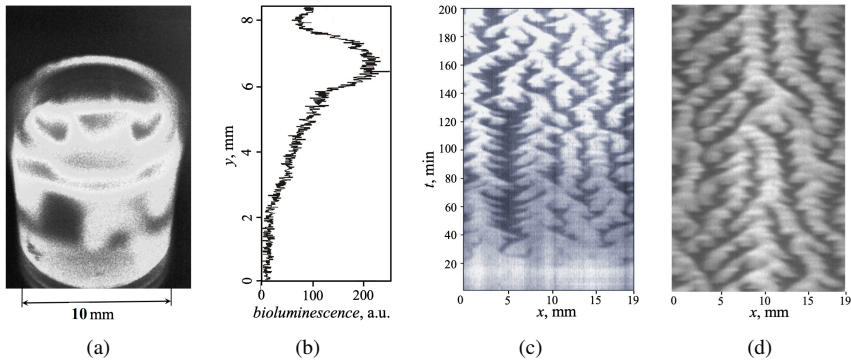
Figure 1. A perspective view of the experimental culture (a) [48], a vertical profile of the bioluminescence intensity measured along the depth (b) [49] and two spatiotemporal plots of the bioluminescence near the three-phase contact line (c) and (d) [49, 52].

The mathematical model and the corresponding numerical model were validated through computational simulations of bioluminescence patterns observed in small, clear glass circular containers [49–51]. Figure 1 shows typical views of the experimental culture, along with the corresponding vertical profile of the bioluminescence intensity measured along the depth, and a spatiotemporal plot of the bioluminescence near the three-phase contact line.

A profile of the vertical distribution n_x of the simulated bacterial density was calculated by integrating the cell density over the tube's circumference and then averaging [6, 49],

$$n_x(y, t) = \frac{1}{l} \int_0^l n(x, y, t) \, \mathrm{d}x, \quad y \in [0, h], \; t \geqslant 0.$$

A quasi-one-dimensional profile of the bacterial density near the three-phase contact line was obtained from the simulated cell densities on the inner lateral surface by integrating over the detectable layer and then averaging [49],

$$n_y(x, t) = \frac{1}{h_0} \int_{h-h_0}^h n(x, y, t) \, \mathrm{d}y, \quad x \in [0, l], \; t \geqslant 0,$$

where $h_0 \in (0, h]$ is the thickness of the detectable layer. In the simulations, it was assumed that the thickness of the detectable layer is equal to half the height of the container, $h_0 = 0.5h$.

For an analysis of the overall dynamics of the bacterial population the average density $\bar{n}$ was also calculated and then visualised,

$$\bar{n}(t) = \frac{1}{lh} \int_0^l \int_0^h n(x, y, t) \, \mathrm{d}y \, \mathrm{d}x, \quad t \geqslant 0.$$
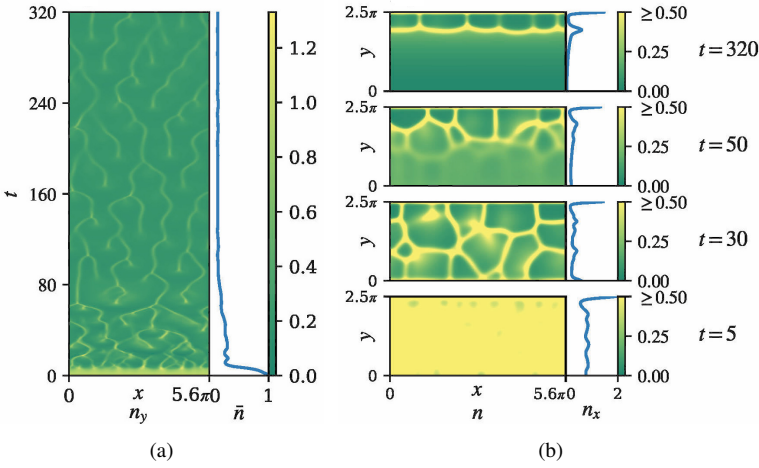
Figure 2. Spatiotemporal plot of the bacterial density n_y along the contact line and average bacterial density $\bar{n}$ (a), the bacterial density n and average bacterial density n_x at different time moments indicated (b), calculated at $\nu = 0$, $\kappa = 1$, $o_{\max} = 1$. The other parameters are as defined in (8).

When viscosity is not taken into consideration ($\nu = 0$) and the excretion of chemoattractant by bacteria is independent of oxygen concentration ($r(o) \equiv 1$, $o_{\max} = 1$), the model (6)–(7) approximates a known model used to simulate the dynamics of bacterial density, self-excreted chemoattractant concentration and oxygen concentration [6, 49]. Assuming $\nu = 0$ and $o_{\max} = 1$, the numerical solution of problem (6)–(7), (2)–(5) was also validated using known numerical solutions [6, 49].

To investigate the impact of gravity and oxygen cut-off on pattern formation, the patterns were simulated at different values of the Schmidt number ν, gravitational force κ and oxygen cut-off parameter $o_{\max}$, while keeping all other parameters constant as described in [49]:

$$
\begin{aligned}
&l = 2\pi 2.8, \quad h = 0.45l, \quad D_n = 0.04, \quad D_o = 0.12, \quad o_{\max} = 1, \\
&\alpha = 1, \quad \beta = 0.73, \quad \lambda = 0.048, \quad \chi = 8.3, \quad \bar{o}_0 = 1, \\
&n_0(x, y) = 1 + \xi(x, y), \quad c_0(x, y) = 0, \quad o_0(x, y) = \bar{o}_0, \\
&\boldsymbol{u}_0(x, y) = 0, \quad (x, y) \in [0, l] \times [0, h],
\end{aligned}
\tag{8}
$$

where ξ is a 10% uniform random spatial perturbation with zero average.

Figure 2 shows simulated patterns at $\nu = 0$, $\kappa = 1$ (no viscosity), $o_{\max} = 1$ (no oxygen cut-off), and the other parameters are as defined in (8).

One can see in Fig. 2 four distinct stages of the pattern formation: initial chaos ($t \lesssim 10$), oxygen saturated solution ($t \lesssim 40$), formation of oxygen gradient ($t \lesssim 80$) and the final quasi-steady state. The chaotic initial stage occurs due to the chosen random spatial perturbation of the initial cell density n_0. Choosing different initial conditions might significantly affect that stage, especially its duration, but the qualitative form of the spatiotemporal patterns depends only slightly on the specificity of the initial conditions [5, 14, 22, 40]. In particular, Deleuze et al. reported that the initial conditions appear to

have a small influence on the number of plumes, but the location of plumes can only be predicted when a very simple initial condition is set up [15]. Figure 2 shows that, eventually, patterns resembling foam emerge from the chaos. Because oxygen is initially uniformly present throughout in the entire solution, the patterns can be observed across the full height of the modelling domain. In models lacking the oxygen component, this state becomes the final quasi-steady state configuration [49], which is far from what is observed experimentally (Fig. 1(a)). Several stages were also experimentally observed in a suspension of the bacterium *Bacillus subtilis*, beginning with upward accumulation and culminating in the hydrodynamic formation of plumes [23, 24, 56]. It was justified that when the vertical density gradient becomes sufficiently large, an overturning instability occurs, analogous to Rayleigh–Bénard convection, eventually developing into complex patterns [23, 24, 45].

As can be seen in Fig. 2, at $t \approx 40$, an oxygen gradient starts to form due to the oxygen consumption defined in (6_3) and boundary conditions (3) and (4). When the oxygen concentration reaches a critically low level at the bottom of the domain, the foam pattern starts to disappear and "moves" up. Eventually, at $(t \approx 80)$, the cell distribution reaches a quasi-steady state and forms a bamboo foam (parallel venation) like pattern [49]. Examining the vertical profile of the cell density (Fig. 2(b)), two peaks are observed: a large peak near the top of the vessel and a smaller peak at approximately one-fifth of the height. Between the two peaks, multiple vertical aggregates of bacteria are observed. The aggregates move horizontally and occasionally merge, but the number of aggregates remains rather stable (5–6 aggregates). This state can be described as quasi-stable.

The simulated bamboo foam-like pattern of the bacteria (Fig. 2(b) and the vertical aggregates (Fig. 2(a)) are similar to those observed in physical experiments (Fig. 1(a)) [49, 50]. However, the vertical distribution of the bacteria differs noticeably. The vertical profiles in Fig. 2(a) show that, in simulations, the peak along the top rim of the modelling domain is larger than the lower peak, which is located at roughly one-fifth of the height. In physical experiments (Fig. 1(b)), however, the lower peak is the larger one. Additionally, in the physical experiments, plumes of bacteria tend to sink downward, a phenomenon that does not occur in the simulation. To achieve simulated patterns closer to the experimental ones, the gravity ($\nu \neq 0$ in (6_4)) and cut-off mechanism ($r(o) \not\equiv 1$, $o_{\max} < 1$) were introduced into the mathematical (1) and corresponding dimensionless (6) models.

4 Results and discussion

In order to investigate the effects of gravity and the cut-off mechanism, bacterial patterns were simulated for different values of three parameters of the dimensionless governing equations (6): the Schmidt number ν, Rayleigh number κ and oxygen cut-off threshold $o_{\max}$.

4.1 Effect of viscosity

The Schmidt number, defined as the ratio of the viscous diffusion rate (kinematic viscosity) to the mass diffusion rate, varies in orders of magnitude in real-world flows [34, 39,
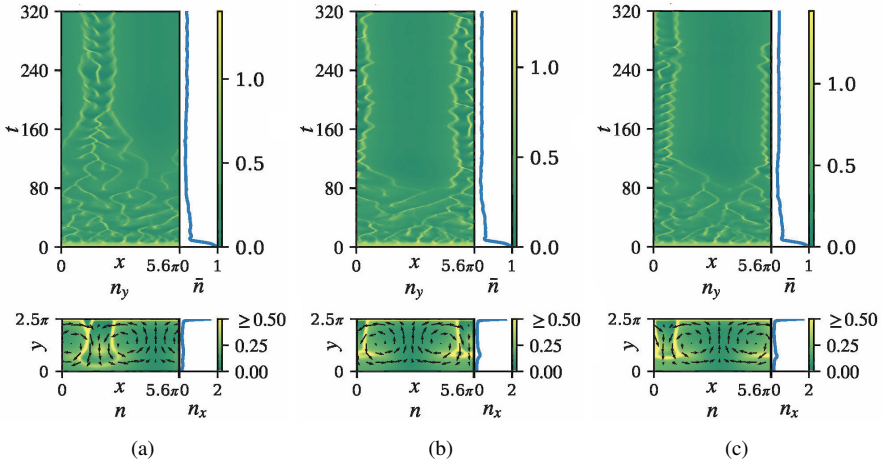
Figure 3. Spatiotemporal plots of the cell density n_y along with the cell densities $\bar{n}$, n and n_x at $t = 300$ and $\kappa = 2$ for three values of the Schmidt number ν: 0.1 (a), 10 (b) and 40 (c). Other parameters are the same as in Fig. 2.

53]. The Schmidt number is often assumed to be in the hundreds or even thousands [13, 32, 37, 39, 53], but numbers as low as 1 or even lower are also used to study flows [34, 53]. Furthermore, increasing the Schmidt number increases the computational cost [34]. Due to the variety of values, the effect of the Schmidt number on the flow remains poorly understood [34].

Bacteria living in the fluid as active particles can reduce the apparent viscosity [33]. A decrease in the viscosity of *E. coli* suspensions to values lower than the viscosity of the suspending fluid was also experimentally determined [20]. The decrease can continue until even a negative apparent viscosity is achieved [33]. Estimations of the diffusion coefficients of bacteria and chemoattractant also vary in an order of magnitude [11,42,58]. These circumstances make it difficult to accurately estimate the Schmidt number.

In order to investigate the effect of the viscosity on gravity-induced population dynamics, the patterns were simulated using different values of the Schmidt number ν, starting from a very small value, and without changing the Rayleigh number κ. Simulated typical spatiotemporal plots and cell density distributions are presented in Fig. 3.

As one can see in spatiotemporal patterns, shown in Fig. 3, that at the beginning of the process, the population behaviour is very similar to that shown in Fig. 2, where the bacteria live in an idealised fluid with no internal friction ($\nu = 0$). In both cases, there are the same three initial stages until the quasi-steady state is reached: initial chaos, oxygen saturation and the formation of an oxygen gradient. Nevertheless, as ν increases, the quasi-steady state is reached at an earlier non-dimensional time moment (Fig. 3). The quasi-steady state time is approximately equal to 120 at $\nu = 40$ (Fig. 3(c)) and at $\nu = 10$ (Fig. 3(b)), and it is approximately equal to 180 at $\nu = 0.1$ (Fig. 3(a)).

After the quasi-steady state is reached ($t \gtrsim 70$), the spatiotemporal patterns of n_y and snapshots of the cell density u are noticeably different from those shown in Fig. 2. Using even very small value of the Schmidt number $\nu = 0.1$ leads to reducing the number of

horizontal aggregates (plumes) from 5–6 in Fig. 2, where $\nu = 0$, to about 3 in Fig. 3(a). Although the number of simulated horizontal aggregates is reduced almost twice, this reduction does not seem as drastic because, in physical experiments, the ratio between the largest and smallest numbers of aggregates was approximately equal to 2 [48, 49, 51, 52]. Figure 3 shows that further increase in ν to 40 affects the patterns only slightly.

In the quasi-stable stage plumes merge and new ones form, however, the number of plumes remains in the range of 2–4. New plumes usually form between two others. In some cases, two plumes start forming at the same time, but they merge during the formation process. The plumes start forming near the bottom and then travel up towards the top of the modelling area. At higher values of ν, the plumes start to form higher up (Fig. 3(c)), at around $3/5$ from the top of the modelling domain. At lower values of ν, the plumes start to form closer to $4/5$ from the top of the modelling domain (Fig. 3(a)).

Figure 3 also shows that in the quasi-steady state, plumes are not horizontally distributed uniformly and can be concentrated at different positions. Due to the continuity of the lateral cylindrical surface and the periodicity of the boundary conditions therefore used on the sides of the domain, the horizontal position can be neglected. However, the concentration of plumes fluctuates only slightly, while in the case of $\nu = 0$, aggregates move horizontally noticeably more freely (Fig. 2). Similar smaller fluctuations are also sometimes observed in physical experiments (Fig. 1(d)).

Further numerical experiments with greater values of the Schmidt number ν showed chaotic patterns. The maximum value of the Schmidt number used in the simulations, $\nu = 40$, seems small compared to values used in other works, e.g., Schmidt numbers of 500 and 1000 were considered typical for *Bacillus subtilis* [13, 56, 60]. In the dimensionless governing equations (6), the model parameter D_n stands for the dimensionless diffusion coefficient of cells, while the incompressible Navier–Stokes equation, coupled with the continuity equations, is usually non-dimensionalized by rescaling the diffusion coefficient of cells to unity [13, 56, 60]. For further rescaling the diffusion coefficient of cells in (6_1) to unity, the Schmidt number ν in (6_4) should be divided by D_n. So, the value $\nu = 40$, used in our simulation, corresponds to $40/0.04 = 1000$ when the dimensionless diffusion coefficient of cells is assumed to be 1. Therefore, the value $\nu = 40$ can be considered suitable for simulating the dynamics of the bacterial population.

4.2 Influence of gravitational forces

In the context of gravity-driven flow at a isothermal conditions, the Rayleigh number describes the potential for buoyancy-driven flow due to concentration differences in the fluid [16, 39, 60]. Deleuze et al. showed that the taxis Rayleigh number, together with the chemotaxis sensitivity, is an important parameter for the occurrence of instabilities in a chemotaxis-diffusion-convection system [15]. Below a critical value of the Rayleigh number the system remains stable [15, 39]. At high Rayleigh numbers, buoyancy forces dominate, leading to convective flow and the formation of gravity-driven plumes, with bacterial taxis primarily driven by gravitation [13, 15, 16, 39].

In governing equations (6), the Rayleigh number κ stands the gravitational forces acting on the fluid due to the bacterial density, which is about 10% higher than that
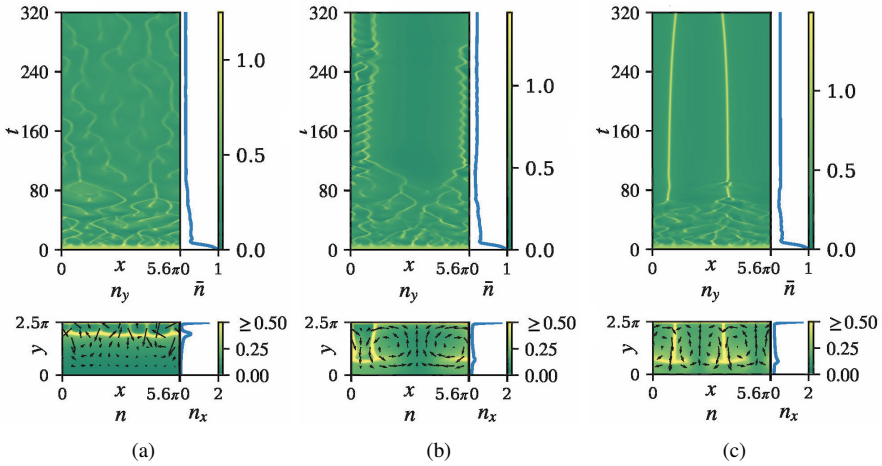
Figure 4. Spatiotemporal plots of the cell density n_y along with the cell densities $\bar{n}$, n and n_x at $t = 300$ and $\nu = 40$ for three values of the Rayleigh number κ: 1 (a), 2 (b) and 5 (c). Other parameters are the same as in Fig. 2.

of the surrounding solution [13, 24]. Initially, bacteria swim up a gradient of oxygen concentration, causing the density of the suspension to become greater at the top than at the bottom. When the vertical density gradient becomes sufficiently large, an overturning convective instability ensues [24].

Depending on the number and specificity of the governing equations, as well as on the non-dimensionalization of the mathematical model, the Rayleigh number can be defined slightly differently [13, 15, 16, 39, 56]. Because of this, the Rayleigh number varies by orders magnitude; its values can range from thousandths to thousands [39]. To investigate the influence of gravitational forces, pattern formations were simulated using various Rayleigh number κ values, starting from unity. Figure 4 shows simulated typical spatiotemporal plots and cell density distributions.

At small value of the Rayleigh number ($\kappa = 1$), even when the Schmidt number is relatively high ($\nu = 40$) (Fig. 4(a)), the cell density n forms a pattern with 5–6 horizontal aggregates similar to the bamboo foam-like structure observed in simulations where gravity is not considered (Fig. 2). In this case, the pattern formation is mainly governed by diffusion and chemotaxis.

At Rayleigh number κ values that are larger than some critical value (Figs. 3, 4(b) and 5 ($\kappa = 1.5$)), vortexes begin to form. A new quasi-stable state is reached, containing 2–3 plumes reaching approximately three quarters of the height. The plumes move intensively, but are concentrated in slightly less than one half of the horizontal area. As κ increases, the quasi-steady state is reached at an earlier time step. The Rayleigh number is critical for gravitational instability and plume formation, which result from the gravitational overturning [16, 31].

The critical value of the Rayleigh number κ for plume formation depends on the value of the Schmidt number ν. While at $\nu = 0.1$ the critical value of κ lies in the interval
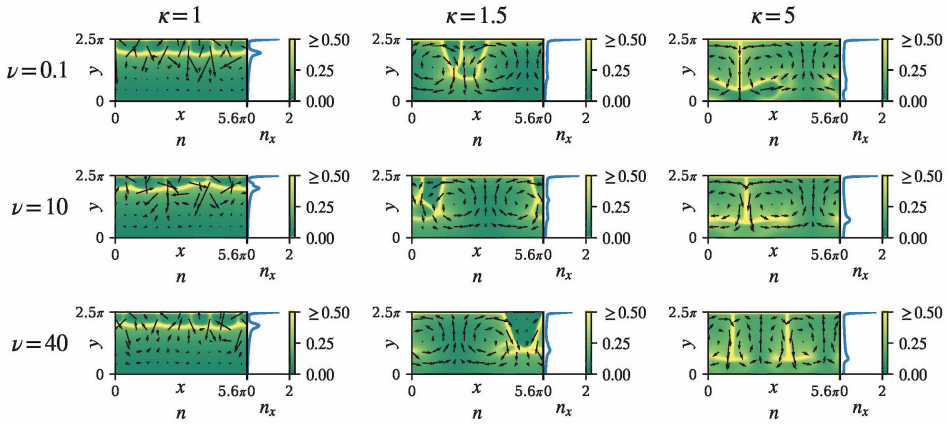
Figure 5. Quasi-steady state bacterial density n and average density n_x, simulated with $\nu = 0.1$, $\nu = 10$ and $\nu = 40$, as indicated by the rows, and $\kappa = 1$, $\kappa = 1.5$ and $\kappa = 5$, as indicated by the columns. Other parameters are the same as in Fig. 2.

$(1.4, 1.5)$, at $\nu = 10$ the critical value is in the interval $(1.1, 1.2)$, and at $\nu = 40$ the critical value is in the interval $(1.0, 1.1)$.

At a high value of the Rayleigh number ($\kappa = 5$, Figs. 4(c) and 5), mushroom-shaped plumes are observed. When the Schmidt number ν is low, the plume retains its quasi-stable nature: new aggregates form near the plume before merging into the plume (Fig. 5 ($\nu = 0.1$ and $\nu = 10$)). Additionally, at higher ν values, several mushroom-shaped plumes can form (Fig. 5 ($\nu = 40$)). As one can see from the spatiotemporal plot depicted in Fig. 4(c), these two plumes practically stagnate, but nevertheless are slowly approaching collision. The plumes converge much more slowly than those observed in cases of smaller values of the Rayleigh number. The arrangement and shape of the plumes generally depend on the Rayleigh number [39, 60].

Similarly to other works [13, 23, 24, 45], the above critical value of the Rayleigh number κ, Figs. 4 and 5 ($\kappa > 1$) show upward fluid flow between the falling plumes in which cells are transported to the surface, where the highest oxygen concentration is maintained. The upward chemotaxis effect activates this flow. This mechanism causes bacteria to accumulate at the surface, where gravity pulls them down and maintains the fluid convection [45]. Increasing the Rayleigh number ($\kappa = 5$) leads to decreasing the chemotaxis effect and changing the shape of the plumes. Then, as also observed by Qiao and Evje [45], plumes fill a larger area in the lower part of the domain.

Similar mushroom-shaped plumes were also observed experimentally by Dunstan et al. in suspensions of nonmotile bacterium *Photobacterium phosphoreum* [16]. Plumes of similar shape were also simulated at high values of Rayleigh number, simulating evaporation-driven convective flows [16, 31]. The plumes were considered an outcome of the gravitational overturning [16].

The simulated patterns containing plumes (Figs. 3–5) are more similar to those observed experimentally (Fig. 1) than the simulated bamboo foam-like structures where gravity is not considered (Fig. 2). However, the simulated 2–3 plumes are notably fewer

than the 5–6 plumes observed experimentally and in simulations where gravity is ignored. Two mushroom-shaped plumes in Figs. 4(c) and 5 are initially distributed approximately uniformly in horizontal direction. As the horizontal interval corresponds to the circumference of the test tube used in physical experiments (Figs. 1(c) and 1(d)), the distance between simulated 2–3, usually 2, plumes is approximately 6.3–9.4 mm, which is 2.5–3 times larger than the value observed experimentally. However, this distance is comparable to the distance (9–10 mm) between adjacent plumes observed in the suspension of *P. phosphoreum* living in a rectangular chamber [16].

The smaller number of simulated plumes (larger distance between adjacent plumes) simulated by using model (6), (7), (2)–(5) can probably explained by the two-dimensionality of the modelling domain: lateral surface of a circular tube. As the bioconvection is intrinsically three-dimensional [32], it seems that two-dimensional domain better reflects the pattern formation in the central transverse section of the circular tube than at the lateral surface. Moreover, the lateral surface attracts bacteria, but this phenomenon is not reflected in the mathematical model. The simulated 2–3 plumes match the number observed in the central transverse section of the circular tube in the physical experiment (Fig. 1(a)) [48–50]. On the other hand, two mushroom-shaped plumes have four edges (fringes, lobes) and can perhaps be considered as a form of evolution of four plumes with increasing Rayleigh number.

4.3 Influence of oxygen cut-off

It is rather well known that the bacterial activity ceases when the oxygen concentration falls below a critical cut-off value [13, 19, 56]. However, it is not entirely clear how this mechanism affects the self-organization of *E. coli* population. Tsimring et al. simulated top-view patterns similar to those observed in *E. coli* experiments by varying the details of the initiation of the chemoattractant emission [55]. Elmas et al. showed that applying a cut-off function based on oxygen concentration to the production of the chemoattractant reduces the density of motile soil oxytactic bacteria *Azospirillum brasilense* near the top of the modelling domain, while the peak around one-fifth of the height remains [19].

To simulate the upper peak of the vertical distribution of cells just below upper surface, as observed in physical experiments (Fig. 1(b)) [48–50], and to investigate how gravity-induced fluid dynamics interact with this modulation, the oxygen cut-off parameter $o_{\max}$ was set to 0.97 while varying the values of parameters ν and κ. The value $o_{\max} = 0.97$ was determined experimentally to remove the upper peak at the top of the modelling domain while preserving the bamboo foam-like structure of the bacterial patterns. Fig. 6 illustrates the simulation results.

As shown in Fig. 6(a), at zero Schmidt number ($\nu = 0$), the four stages observed in the absence of oxygen cut-off (Fig. 2) are still present. However, an additional stage, namely vertical aggregate formation, appears before the quasi-stable state. The bacterial patterns during the stages, however, are different. Due to the hard cut-off function $r(o)$, during the initial chaotic stage ($t \lesssim 10$) a noticeable pattern of reappearing horizontal aggregation of bacteria emerges. The oxygen-saturated solution stage ($t \lesssim 30$) and the subsequent oxygen gradient formation stage ($t \lesssim 70$) are shorter. Before a quasi-stable
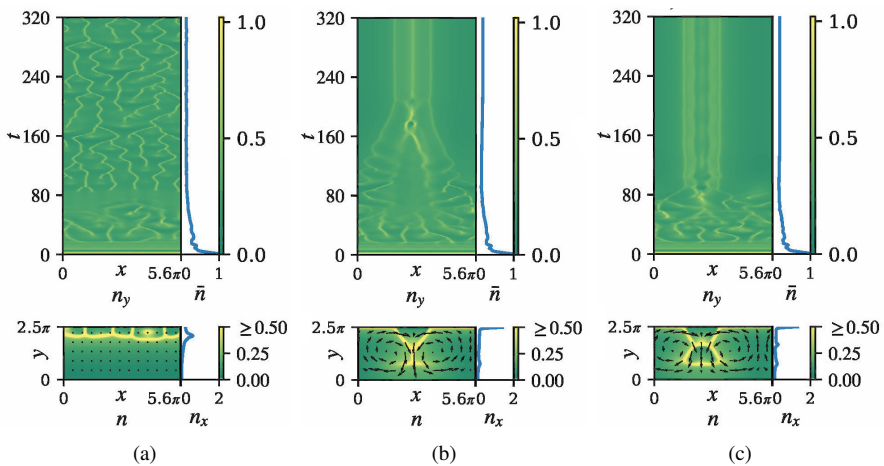
Figure 6. Spatiotemporal plots of the cell density n_y along with the cell densities $\bar{n}$, n and n_x at $t = 320$, $\kappa = 1.5$ and $o_{\max} = 0.97$ for three values of ν: 0 (a), 0.1 (b) and 40 (c). Other parameters are the same as in Fig. 2.

state is reached, a vertical aggregate formation stage occurs ($t \lesssim 90$). During this stage, we observe a single horizontal aggregate at approximately one-fifth of the container's height. This corresponds to the smaller peak in the vertical profile of the baseline model's quasi-steady state. Eventually, 4 to 6 vertical aggregates form between the top of the container and the horizontal aggregate. These aggregates move horizontally and occasionally merge, however, their number remains stable, similar to when no oxygen cut-off is applied. Notably, the top peak in the vertical profile view disappears.

When $\nu > 0$ (Figs. 6(b) and 6(c)), vertical aggregates take the form of plumes. Plume formation starts at approximately the same time as aggregate formation at $\nu = 0$, but takes significantly longer time to develop. When $\nu = 0.1$ and $\kappa = 1.5$, plume formation ends at $t \approx 210$ (Fig. 6(b)). When $\nu = 48$ and $\kappa = 1.5$, plume formation ends at $t \approx 90$ (Fig. 6(c)). At lower ν values (Fig. 6(b)), instead of a quasi-stable state, a stable state is reached. Two plumes form at the top of the modelling domain. The plumes merge at around one-third of the height from the top of the modelling domain.

At lower values of ν ($\nu = 0.1$, Fig. 6(b)), the two plumes merge and continue as one mushroom-shaped plume that reaches $4/5$ of the way from the top of the modelling domain. At higher values of ν ($\nu = 40$, Fig. 6(c)), a horizontal aggregate forms at the merging height, connecting the two plumes. Two new plumes then extend downward to $4/5$ of the way from the top of the modelling domain. At this height, another horizontal aggregate forms between the plumes. In this case, the lower plumes appear as a continuation of the plumes in the top half of the modelling domain.

When the oxygen cut-off value $o_{\max} < 1$, one can observe that no bacteria are present between the plumes at the contact line ($y = h$). This happens because the bacteria at high concentration of oxygen at the top of the modelling domain does not produce chemoattractant and moves downward due to chemotaxis. However, in other regions of the domain, vortexes formed by gravity push the bacteria towards the top. This

explains the difference in the vertical profiles in the case of $\nu = 0$ (Fig. 6(a)) and $\nu > 0$ (Figs. 6(b) and 6(c)).

5   Conclusions

We have demonstrated that the reaction–diffusion–chemotaxis model, coupled with the incompressible Navier–Stokes equations and a cut-off mechanism, can simulate mushroom-shaped plume-like patterns resembling bioluminescence patterns (Figs. 3–6) that represent the self-organization of luminous *E. coli* bacteria.

Viscosity and gravitational forces, represented in the mathematical model (6)–(7), (2)–(5) by the Schmidt number ν and Rayleigh number κ, respectively, play a crucial role in plume formation.

Plumes form in simulated bacterial patterns only when the Rayleigh number κ exceeds a critical value, which depends on the Schmidt number. The critical value of Rayleigh number decreases as the Schmidt number increases. The simulated plumes are predominantly concentrated horizontally in the lower half of the two-dimensional modelling domain. However, in physical experiments, more plumes were distributed on the upper side of the container.

When the Rayleigh number κ exceeds the critical value, the Schmidt number ν significantly affects the time required to reach the quasi-stable state. As the Schmidt number increases, plumes form earlier. Once the simulation reaches a quasi-stable state, the Schmidt number has only a small effect on the plume form, even for large differences in parameter ν values (Figs. 3 and 5). Numerical simulation can be used to determine the parameters that provide a balance between chemotaxis and gravity to achieve plume patterns.

The application of the cut-off mechanism contributes to shifting the peak of bacterial concentration from the top surface to just below that surface (Fig. 6), as observed in physical experiments [48–50]. In the case of the Schmidt number of $\nu = 0$, when the oxygen cut-off parameter $o_{\max}$ is lower than a critical value, the upper peak in the vertical profile view disappears, and only the lower peak remains. This observation agrees well with the physical experiments. However, if $\nu > 0$, the peak shifts to the top of the simulated area. This occurs due to gravity induced vortices in the simulated fluid.

Although the two-dimensional mathematical model (6)–(7), (2)–(5), which couples bacterial chemotaxis with gravitational forces, is useful for simulating patterns similar to the experimentally observed and for studying the effects of gravity on pattern formation, a more precise and sophisticated three-dimensional computational model should be developed to study the bacterial pattern formation in detail in a luminous *E. coli* colony.

References

1. J. Adler, Chemoreceptors in bacteria, *Science*, **166**(3913):1588–1597, 1969, https://doi.org/10.1126/science.166.3913.1588.

2. M. Adler, M. Erickstad, E. Gutierrez, A. Groisman, Studies of bacterial aerotaxis in a microfluidic device, *Lab Chip*, **12**(22):4835–4847, 2012, https://doi.org/10.1039/c2lc21006a.

3. M. Ardré, D. Dufour, P.B. Rainey, Causes and biophysical consequences of cellulose production by *Pseudomonas fluorescens* SBW25 at the air-liquid interface, *J. Bacteriol.*, **201**(18):e00110–19, 2019, https://doi.org/10.1128/jb.00110-19.

4. G. Arumugam, J. Tyagi, Keller–Segel chemotaxis models: A review, *Acta Appl. Math.*, **171**(1): 6, 2021, https://doi.org/10.1007/s10440-020-00374-2.

5. L.V. Ballestra, Modeling economic growth with spatial migration: A stability analysis of the long-run equilibrium based on semigroup theory, *J. Math. Anal. Appl.*, **531**(1):127794, 2024, https://doi.org/10.1016/j.jmaa.2023.127794.

6. R. Baronas, Ž. Ledas, R. Šimkus, Computational modeling of the bacterial self-organization in a rounded container: The effect of dimensionality, *Nonlinear Anal. Model. Control*, **20**(4):603–620, 2015, https://doi.org/10.15388/NA.2015.4.10.

7. R. Baronas, R. Šimkus, Modeling the bacterial self-organization in a circular container along the contact line as detected by bioluminescence imaging, *Nonlinear Anal. Model. Control*, **16**(3):270–282, 2011, https://doi.org/10.15388/NA.16.3.14093.

8. N. Bellomo, N. Outada, J. Soler, Y. Tao, M. Winkler, Chemotaxis and cross-diffusion models in complex environments: Models and analytic problems toward a multiscale vision, *Math. Models Methods Appl. Sci.*, **32**(4):713–792, 2022, https://doi.org/10.1142/S0218202522500166.

9. H.C. Berg, D.A. Brown, Chemotaxis in *Escherichia coli* analysed by three-dimensional tracking, *Nature*, **239**(5374):500–504, 1972, https://doi.org/10.1038/239500a0.

10. M. Bisi, M. Groppi, G. Martalò, C. Soresina, A chemotaxis reaction–diffusion model for multiple sclerosis with Allee effect, *Ric. Mat.*, **73**(1):29–46, 2024, https://doi.org/10.1007/s11587-023-00806-9.

11. M.P. Brenner, L.S. Levitov, E.O. Budrene, Physical mechanisms for chemotactic pattern formation by bacteria, *Biophys. J.*, **74**(4):1677–1693, 1998, https://doi.org/10.1016/S0006-3495(98)77880-4.

12. E.O. Budrene, H.C. Berg, Dynamics of formation of symmetrical patterns by chemotactic bacteria, *Nature*, **376**(6535):49–53, 1995, https://doi.org/10.1038/376049a0.

13. A. Chertock, K. Fellner, A. Kurganov, A. Lorz, P.A. Markowich, Sinking, merging and stationary plumes in a coupled chemotaxis-fluid model: A high-resolution numerical approach, *J. Fluid Mech.*, **694**:155–190, 2012, https://doi.org/10.1017/jfm.2011.534.

14. R. Čiegis, A. Bugajev, Numerical approximation of one model of bacterial self-organization, *Nonlinear Anal. Model. Control*, **17**(3):253–270, 2012, https://doi.org/10.15388/NA.17.3.14054.

15. Y. Deleuze, C.Y. Chiang, M. Thiriet, T.W.H. Sheu, Numerical study of plume patterns in a chemotaxis–diffusion–convection coupling system, *Comput. Fluids*, **126**:58–70, 2016, https://doi.org/10.1016/j.compfluid.2015.10.018.

16. J. Dunstan, K.J. Lee, Y. Hwang, S.F. Park, R.E. Goldstein, Evaporation-driven convective flows in suspensions of nonmotile bacteria, *Phys. Rev. Fluids*, **3**:123102, 2018, `https://doi.org/10.1103/PhysRevFluids.3.123102`.

17. S.I. Ei, H. Izuhara, M. Mimura, Spatio-temporal oscillations in the Keller–Segel system with logistic growth, *Physica D*, **277**:1–21, 2014, `https://doi.org/10.1016/j.physd.2014.03.002`.

18. M. Eisenbach, *Chemotaxis*, Imperial College Press, London, 2004.

19. M. Elmas, V. Alexiades, L. O'Neal, G. Alexandre, Modeling aerotaxis band formation in azospirillum brasilense, *BMC Microbiol.*, **19**:101, 2019, `https://doi.org/10.1186/s12866-019-1468-9`.

20. J. Gachelin, G. Miño, H. Berthet, A. Lindner, A. Rousselet, É. Clément, Non-Newtonian viscosity of *Escherichia coli* suspensions, *Phys. Rev. Lett.*, **110**(26):268103, 2013, `https://doi.org/10.1103/PhysRevLett.110.268103`.

21. T. Hillen, K.J. Painter, A user's guide to PDE models for chemotaxis, *J. Math. Biol.*, **58**(1–2):183–217, 2009, `https://doi.org/10.1007/s00285-008-0201-3`.

22. T. Hillen, J. Zielinski, K.J. Painter, Merging-emerging systems can describe spatio-temporal patterning in a chemotaxis model, *Discrete Contin. Dyn. Syst., Ser. B*, **18**(10):2513–2536, 2013, `https://doi.org/10.3934/dcdsb.2013.18.2513`.

23. A.J. Hillesdon, T.J. Pedley, Bioconvection in suspensions of oxytactic bacteria: Linear theory, *J. Fluid Mech.*, **324**:223–259, 1996, `https://doi.org/10.1017/S0022112096007902`.

24. A.J. Hillesdon, T.J. Pedley, O. Kessler, The development of concentration gradients in a suspension of chemotactic bacteria, *Bull. Math. Biol.*, **57**:299–344, 1995, `https://doi.org/10.1007/BF02460620`.

25. J.S. Hong, K.H. Ahn, G.G. Fuller, M.C. Kim, Evaporation-driven gravitational instability in the liquid layer of a polymer solution: Theoretical and numerical studies, *Phys. Fluids*, **35**(6):064103, 2023, `https://doi.org/10.1063/5.0152147`.

26. D. Horstmann, From 1970 until present: The Keller-Segel model in chemotaxis and its consequences, *Jahresber. Dtsch. Math.-Ver.*, **105**(3):103–165, 2003.

27. F. Ivančić, T.W.H. Sheu, M. Solovchuk, The free surface effect on a chemotaxis–diffusion–convection coupling system, *Comput. Methods Appl. Mech. Eng.*, **356**:387–406, 2019, `https://doi.org/10.1016/j.cma.2019.07.030`.

28. R. Johansson, *Numerical Python: Scientific Computing and Data Science Applications with Numpy, SciPy and Matplotlib*, Apress, Berkeley, CA, 2019, `https://doi.org/10.1007/978-1-4842-4246-9`.

29. E.F. Keller, L.A. Segel, Initiation of slime mold aggregation viewed as an instability, *J. Theor. Biol.*, **26**(3):399–415, 1970, `https://doi.org/10.1016/0022-5193(70)90092-5`.

30. E.F. Keller, L.A. Segel, Model for chemotaxis, *J. Theor. Biol.*, **30**(2):225–234, 1971, `https://doi.org/10.1016/0022-5193(71)90050-6`.

31. M.C. Kim, Onset of evaporation-driven gravitational instability in a saline solution, *Korean J. Chem. Eng.*, **38**(1):144–151, 2021, `https://doi.org/10.1007/s11814-020-0673-4`.

32. H.G. Lee, J. Kim, Numerical investigation of falling bacterial plumes caused by bioconvection in a three-dimensional chamber, *Eur. J. Mech., B, Fluids*, **52**:120–130, 2015, `https://doi.org/10.1016/j.euromechflu.2015.03.002`.

33. A. Loisy, J. Eggers, T.B. Liverpool, Active suspensions have nonmonotonic flow curves and multiple mechanical equilibria, *Phys. Rev. Lett.*, **121**:018001, Jul 2018, `https://doi.org/10.1103/PhysRevLett.121.018001`.

34. C.R. Marshall, R.M. Dorrell, S. Dutta, G.M. Keevil, J. Peakall, S.M. Tobias, The effect of Schmidt number on gravity current flows: The formation of large-scale three-dimensional structures, *Phys. Fluids*, **33**(10):106601, 2021, `https://doi.org/10.1063/5.0064386`.

35. B.C. Mazzag, I.B. Zhulin, A. Mogilner, Model of bacterial band formation in aerotaxis, *Biophys. J.*, **85**(6):3558–3574, 2003, `https://doi.org/10.1016/s0006-3495(03)74775-4`.

36. J.D. Murray, *Mathematical Biology II: Spatial Models and Biomedical Applications,* 3rd ed., Springer, New York, 2003, `https://doi.org/10.1007/b98869`.

37. N. Murugan, A. Roy, Instability of a thin film of chemotactic active suspension, *J. Fluid Mech.*, **995**:A11, 2023, `https://doi.org/10.1017/jfm.2022.1063`.

38. M.R. Myerscough, P.K. Maini, K.J. Painter, Pattern formation in a generalized chemotactic model, *Bull. Math. Biol.*, **60**(1):1–26, 1998, `https://doi.org/10.1006/bulm.1997.0010`.

39. Y. Nagata, A. Minakawa, T. Kawamura, Classification of two-dimensional convection patterns in density instability model of bioconvection, *Theor. Appl. Mech. Jpn.*, **64**:73–77, 2018, `https://doi.org/10.11345/nctam.64.73`.

40. K.J. Painter, Mathematical models for chemotaxis and their applications in self-organisation phenomena, *J. Theor. Biol.*, **481**:162–182, 2019, `https://doi.org/10.1016/j.jtbi.2018.06.019`.

41. T.J. Pedley, J.O. Kessler, Hydrodynamic phenomena in suspensions of swimming microorganisms, *Annu. Rev. Fluid Mech.*, **24**:313–358, 1992, `https://doi.org/10.1146/annurev.fl.24.010192.001525`.

42. N. Perry, Experimental validation of a critical domain size in reaction-diffusion systems with *Escherichia coli* populations, *J. R. Soc. Interface*, **2**(4):379–387, 2005, `https://doi.org/10.1098/rsif.2005.0054`.

43. A.A. Polezhaev, R.A. Pashkov, A.I. Lobanov, I.B. Petrov, Spatial patterns formed by chemotactic bacteria *Escherichia coli*, *Int. J. Dev. Biol.*, **50**:309–314, 2006, `https://doi.org/10.1387/ijdb.052048ap`.

44. W.H. Press, S.A. Teukolsky, W.T. Vetterling, B.P. Flannery, *Numerical Recipes: The Art of Scientific Computing,* 3rd ed., Cambridge Univ. Press, Cambridge, 2007.

45. Y. Qiao, S. Evje, A general cell–fluid Navier–Stokes model with inclusion of chemotaxis, *Math. Models Methods Appl. Sci.*, **30**(06):1167–1215, 2020, `https://doi.org/10.1142/S0218202520400096`.

46. A.A. Samarskii, *The Theory of Difference Schemes*, Marcel Dekker, New York, Basel, 2001, `https://doi.org/10.1201/9780203908518`.

47. J. Shioi, C.V. Dang, B.L. Taylor, Oxygen as attractant and repellent in bacterial chemotaxis, *J. Bacteriol.*, **169**(7):3118–3123, 1987, `https://doi.org/10.1128/jb.169.7.3118-3123.1987`.

48. R. Šimkus, R. Baronas, Metabolic self-organization of bioluminescent *Escherichia coli*, *Luminescence*, **26**(6):716–721, 2011, `https://doi.org/10.1002/bio.1303`.

49. R. Šimkus, R. Baronas, Ž. Ledas, A multi-cellular network of metabolically active *E. coli* as a weak gel of living janus particles, *Soft Matter*, **9**(17):4489–4500, 2013, `https://doi.org/10.1039/c3sm27786k`.

50. R. Šimkus, V. Kirejev, R. Meškienė, R. Meškys, Torus generated by *Escherichia coli*, *Exp. Fluids*, **46**(2):365–369, 2009, `https://doi.org/10.1007/s00348-008-0598-x`.

51. R. Šimkus, R. Meškienė, A. Aučynaitė, Ž. Ledas, R. Baronas, R. Meškys, Phoretic interactions and oscillationsin active suspensions of growing *Escherichia coli*, *R. Soc. Open Sci.*, **5**(5):180008, 2018, `https://doi.org/10.1098/rsos.180008`.

52. R. Šimkus, R. Meškienė, Ž. Ledas, R. Baronas, R. Meškys, Microtiter plate tests for segregation of bioluminescent bacteria, *Luminescence*, **31**(6):127–134, 2016, `https://doi.org/10.1002/bio.2934`.

53. N. Takagaki, R. Kurose, A. Kimura, S. Komori, Effect of Schmidt number on mass transfer across a sheared gas-liquid interface in a wind-driven turbulence, *Sci. Rep.*, **33**:37059, 2016, `https://doi.org/10.1038/srep37059`.

54. A.D.O. Tisbury, D.J. Needham, A. Tzella, The evolution of traveling waves in a KPP reaction-diffusion model with cut-off reaction rate. I. Permanent form traveling waves, *Stud. Appl. Math.*, **146**(2):301–329, 2021, `https://doi.org/10.1111/sapm.12337`.

55. L. Tsimring, H. Levine, I. Aranson, E. Ben-Jacob, I. Cohen, O. Shochet, W.N. Reynolds, Aggregation patterns in stressed bacteria, *Phys. Rev. Lett.*, **75**(9):1859–1862, 1995, `https://doi.org/10.1103/PhysRevLett.75.1859`.

56. I. Tuval, L. Cisneros, C. Dombrowski, C.W. Wolgemuth, J. Kessler, R.E. Goldstein, Bacterial swimming and oxygen transport near contact lines, *Proc. Natl. Acad. Sci. USA*, **102**(7):2277–2282, 2005, `https://doi.org/10.1073/pnas.0406724102`.

57. R. Tyson, S.R. Lubkin, J.D. Murray, A minimal mechanism for bacterial pattern formation, *Proc. R. Soc. Lond. B*, **266**(1416):299–304, 1999, `https://doi.org/10.1098/rspb.1999.0637`.

58. R. Tyson, L.G. Stern, R.J. LeVeque, Fractional step methods applied to a chemotaxis model, *J. Math. Biol.*, **41**(5):455–475, 2000, `https://doi.org/10.1007/s002850000038`.

59. D.E. Woodward, R. Tyson, M.R. Myerscough, J.D. Murray, E.O. Budrene, H.C. Berg, Spatio-temporal patterns generated by *Salmonella Typhimurium*, *Biophys. J.*, **68**(5):2181–2189, 1995, `https://doi.org/10.1016/S0006-3495(95)80400-5`.

60. H. Yanaoka, T. Nishimura, Pattern wavelengths and transport characteristics in three-dimensional bioconvection generated by chemotactic bacteria, *J. Fluid Mech.*, **952**:A13, 2022, `https://doi.org/10.1017/jfm.2022.898`.

61. A. Ziepke, I. Maryshev, I.S. Aranson, E. Frey, Multi-scale organization in communicating active matter, *Nat. Commun.*, **13**(1):6727, 2022, `https://doi.org/10.1038/s41467-022-34484-2`.